









# The Remarkable X-ray Spectra and Variability of the Ultraluminous Weak-Line Quasar SDSS J1521+5202

SHOUYI WANG <sup>1,2,3</sup> W. N. BRANDT <sup>3,4,5</sup> BIN LUO <sup>1,2</sup> ZHIBO YU <sup>3,4</sup> FAN ZOU <sup>3,4</sup> JIAN HUANG <sup>1,2</sup>  
QINGLING NI <sup>6</sup> AND FABIO VITO <sup>7</sup>

<sup>1</sup>*School of Astronomy and Space Science, Nanjing University, Nanjing, Jiangsu 210093, People's Republic of China*

<sup>2</sup>*Key Laboratory of Modern Astronomy and Astrophysics (Nanjing University), Ministry of Education, Nanjing 210093, People's Republic of China*

<sup>3</sup>*Department of Astronomy and Astrophysics, 525 Davey Lab, The Pennsylvania State University, University Park, PA 16802, USA*

<sup>4</sup>*Institute for Gravitation and the Cosmos, The Pennsylvania State University, University Park, PA 16802, USA*

<sup>5</sup>*Department of Physics, 104 Davey Lab, The Pennsylvania State University, University Park, PA 16802, USA*

<sup>6</sup>*Max-Planck-Institut für extraterrestrische Physik (MPE), Gießenbachstraße 1, D-85748 Garching bei München, Germany*

<sup>7</sup>*INAF – Osservatorio di Astrofisica e Scienza dello Spazio di Bologna, Via Gobetti 93/3, I-40129 Bologna, Italy*

## ABSTRACT

We present a focused X-ray and multiwavelength study of the ultraluminous weak-line quasar (WLQ) SDSS J1521+5202, one of the few X-ray weak WLQs that is amenable to basic X-ray spectral and variability investigations. J1521+5202 shows striking X-ray variability during 2006–2023, by up to a factor of  $\approx 32$  in 0.5–2 keV flux, and our new 2023 Chandra observation caught it in its brightest X-ray flux state to date. Concurrent infrared/optical observations show only mild variability. The 2023 Chandra spectrum can be acceptably described by a power law with intrinsic X-ray absorption, and it reveals a nominal intrinsic level of X-ray emission relative to its optical/ultraviolet emission. In contrast, an earlier Chandra spectrum from 2013 shows apparent spectral complexity that is not well fit by a variety of models, including ionized-absorption or standard Compton-reflection models. Overall, the observations are consistent with the thick-disk plus outflow model previously advanced for WLQs, where a nominal level of underlying X-ray emission plus variable absorption lead to the remarkable observed X-ray variability. In the case of J1521+5202 it appears likely that the outflow, and not the thick disk itself, lies along our line-of-sight and causes the X-ray absorption.

*Keywords:* : High energy astrophysics; Active galaxies; Quasars; X-ray active galactic nuclei;

## 1. INTRODUCTION

### 1.1. Observations and Modeling of Weak-Line Quasars

Weak-line quasars are a sub-class of type 1 quasars that continue to provide insights into quasar accretion physics and structure. They are blue, luminous quasars with remarkably weak and often highly blueshifted high-ionization emission lines. For example, their broad C IV rest-frame equivalent widths (REWs) are  $\lesssim 10\text{--}15 \text{ \AA}$ , and their C IV blueshifts can reach  $5000\text{--}10000 \text{ km s}^{-1}$  (e.g., Fan et al. 1999; Diamond-Stanic et al. 2009; Wu et al. 2012). Most WLQs are radio quiet.

X-ray observations of WLQs have played an essential role in revealing their nature (e.g., Wu et al. 2011; Luo et al. 2015; Marlar et al. 2018; Ni et al. 2018, 2022). WLQs show a number of remarkable X-ray properties, as recently detailed in Section 1 of Ni et al. (2022). Briefly, WLQs show an unusually

broad range of X-ray luminosities compared to those expected from their optical/ultraviolet (UV) luminosities or spectral energy distributions, with about half of WLQs being notably X-ray weak. The X-ray luminosity relative to the optical/UV luminosity is generally assessed using the  $\alpha_{\text{OX}}$  and  $\Delta\alpha_{\text{ox}}$  parameters.  $\alpha_{\text{OX}}$  is the slope of a nominal power law connecting the rest-frame 2500  $\text{\AA}$  and 2 keV monochromatic luminosities, i.e.,  $\alpha_{\text{ox}} = 0.3838 \log(L_{2 \text{ keV}}/L_{2500 \text{ \AA}})$ , and this quantity is significantly correlated with  $L_{2500 \text{ \AA}}$  (e.g., Steffen et al. 2006; Just et al. 2007). We also define  $\Delta\alpha_{\text{ox}} = \alpha_{\text{ox}}(\text{Observed}) - \alpha_{\text{ox}}(L_{2500 \text{ \AA}})$ , which quantifies the deviation of the observed X-ray luminosity relative to that expected from the  $\alpha_{\text{OX}}\text{--}L_{2500 \text{ \AA}}$  correlation.  $\Delta\alpha_{\text{ox}}$  can be used to derive factors of X-ray weakness following  $f_{\text{weak}} = 403^{-\Delta\alpha_{\text{ox}}}$ . X-ray spectral analyses of the half of WLQs with nominal-strength (relative to

their optical/UV emission given by the  $\alpha_{\text{OX}}-L_{2500 \text{ \AA}}$  relation) X-ray emission show steep power-law continua (with photon indices of  $\Gamma = 2.0-2.4$ ), suggesting high Eddington ratios ( $L/L_{\text{Edd}}$ ). In contrast, X-ray spectral analyses of the half of WLQs that are X-ray weak show hard X-ray spectra on average (effective  $\langle \Gamma \rangle \approx 1.2-1.4$ ), suggesting high levels of intrinsic X-ray absorption (at least  $N_{\text{H}} \approx 10^{23} \text{ cm}^{-2}$ ) and probably also Compton reflection. Such heavy X-ray absorption is surprising given these quasars’ type 1 nature and blue optical/UV continua without Broad Absorption Lines (BALs) or other strong UV absorption features.

Based upon the available X-ray and multiwavelength results, a basic working model has been advanced for WLQs that has the potential to explain, in a simple and unified manner, their weak UV lines, their X-ray properties, and their other multiwavelength properties (e.g., Wu et al. 2011; Luo et al. 2015; Ni et al. 2018, 2022); Figure 1 of Ni et al. (2018) shows a relevant schematic of the model. To explain the weak UV lines, this model relies upon small-scale “shielding” of ionizing EUV/X-ray photons that prevents them from reaching the broad emission-line region (BELR). The shielding material is likely the geometrically and optically thick inner accretion disk, and its associated outflow, expected for a quasar accreting with high  $L/L_{\text{Edd}}$ —the thick disk and its outflow will be abbreviated as “TDO”. The shielding is also responsible for the X-ray weakness and apparent absorption seen in about half of WLQs. When our line of sight intercepts the shield, we see an X-ray weak WLQ; when it misses the shield, we observe an X-ray normal WLQ. In both cases, ionizing EUV/X-ray photons are prevented from reaching the (largely equatorial and unobscured) high-ionization BELR, and the optical/UV continuum remains unobscured. In this shielding model, strong X-ray flux and spectral variability could arise if the line-of-sight absorption column density and/or covering factor of the shield varies, e.g., due to motions of the TDO. Indeed, a few examples of remarkably strong X-ray variability discovered among WLQs have been explained with TDO variations (e.g., Miniutti et al. 2012; Ni et al. 2020; Liu et al. 2022). In extreme cases, the observed X-ray flux could vary between X-ray weak (highly absorbed) and X-ray normal (completely unabsorbed) states.

## 1.2. The Ultraluminous Weak-Line Quasar J1521+5202

X-ray spectral and variability analyses of the critical X-ray weak WLQs are challenging, owing to the inevitably limited numbers of detected counts (generally 10 or fewer) in the available observations (e.g., Ni

et al. 2022). Most of the X-ray spectral results for these objects have been derived only in an average sense by stacking sets of WLQs together, which can confuse interpretation if spectral diversity is present among the objects stacked.

Moderate-quality X-ray spectral analyses have only been possible for the singular object J1521+5202, an X-ray weak WLQ at  $z = 2.24$  that is one of the few most-luminous quasars in the Universe in the optical/UV with  $M_i = -30.2$  (Schneider et al. 2005). The exceptional luminosity of J1521+5202 makes it possible to obtain X-ray spectra despite its clear X-ray weakness by a factor of  $f_{\text{weak}} \approx 35$  ( $\alpha_{\text{ox}} = -2.42$ ,  $\Delta\alpha_{\text{ox}} = -0.59$ , and observed  $L_{2-10 \text{ keV}} = 3 \times 10^{44} \text{ erg s}^{-1}$ ; Luo et al. 2015). The rest-frame optical/UV spectroscopic properties of J1521+5202 are representative of those of WLQs. For example, its C IV line is strikingly weak ( $\text{REW} = 9.1 \pm 0.6 \text{ \AA}$ ) but is clearly broad ( $\text{FWHM} = 11700 \pm 800 \text{ km s}^{-1}$ ) and blueshifted (by  $9300 \pm 610 \text{ km s}^{-1}$ ). Based on (admittedly uncertain) virial estimates using its H $\beta$  line, its black-hole mass is  $\approx 6 \times 10^9 M_{\odot}$  with  $L/L_{\text{Edd}} \approx 1-2$  (Wu et al. 2011; Luo et al. 2015). Similar to the other X-ray weak WLQs, J1521+5202 does not show any BALs in its UV spectrum. It is a radio-quiet quasar with  $R < 0.2$ , where  $R = f_{5 \text{ GHz}}/f_{4400 \text{ \AA}}$ .

A Chandra Advanced CCD Imaging Spectrometer (ACIS) spectrum of J1521+5202 (37.2 ks exposure; 92 counts), obtained in October 2013, revealed extraordinary properties for a highly luminous, type 1, and non-BAL quasar (Luo et al. 2015). Fitting a power-law model with Galactic absorption (using the Cash statistic) returned a photon index of  $\Gamma = 0.6 \pm 0.2$  for the rest-frame 3–20 keV band. This very hard X-ray spectrum suggests the X-ray weakness of J1521+5202 is likely due to strong intrinsic X-ray absorption.

## 1.3. Paper Overview and Definitions

In this paper, we present the most complete X-ray spectral and variability study of J1521+5202 to date, aiming to understand better the nature of this remarkable WLQ and WLQs generally. We have obtained a new Chandra ACIS observation (29.7 ks exposure), and we also collect all available archival X-ray results for this quasar over the past 18 yr to examine its long-term X-ray variability. We furthermore compare with its long-term optical and infrared (IR) variability. In Section 2 we present the X-ray observations utilized and their reduction, and in Section 3 we present the derived X-ray and multiwavelength properties of J1521+5202. Section 4 presents a summary of the results with relevant discussion.

Throughout this paper, we use J2000 coordinates and a cosmology with  $H_0 = 70 \text{ km s}^{-1} \text{ Mpc}^{-1}$ ,  $\Omega_\Lambda = 0.7$ , and  $\Omega_M = 0.3$ .

## 2. X-RAY OBSERVATIONS AND DATA REDUCTION

### 2.1. *Chandra Observations*

J1521+5202 was observed by Chandra ACIS-S three times in June 2006, October 2013, and February 2023. Table 1 provides the basic information for these Chandra observations. The results from the first and second observations were originally presented in Just et al. (2007) and Luo et al. (2015), respectively, and we present results from the third observation here for the first time.

Using the Chandra Interactive Analysis of Observations (CIAO; v4.15) tools, we analyze the Chandra data. We first run the CHANDRA\_REPRO script for each observation to generate a new level 2 event file. Then, we run the DEFLARE script and use an iterative  $3\sigma$  clipping algorithm to filter potential background flares. The cleaned exposure times are 4.1 ks, 37.2 ks, and 29.7 ks in 2006, 2013, and 2023, respectively. We use the SPEXTRACT tool to extract source spectra using a circular source region with a radius of  $4''$  centered on the quasar X-ray position. The background spectra are extracted from an annular region centered on the quasar position with a  $6''$  inner radius and a  $15''$  outer radius. We group the spectra with at least one count per bin for spectral fitting. The spectra have  $\approx 3$ , 92, and 114 total counts in the full band (0.5–8 keV) in 2006, 2013, and 2023, respectively. We then assess the source-detection significance via computing the binomial no-source probability (e.g., Luo et al. 2015; Liu et al. 2022),  $P_B$ , which is defined as

$$P_B = \sum_{X=S}^N \frac{N!}{X!(N-X)!} p^X (1-p)^{N-X}. \quad (1)$$

In Equation (1),  $S$  is the total number of counts in the source region in the full band,  $B$  is the total number of counts in the background region,  $N = S + B$ , and  $p = 1 / (1 + \text{BACKSCAL})$ , with BACKSCAL being the ratio of the background and source region areas. The computed  $P_B$  values in these three Chandra observations are all smaller than 0.01, corresponding to  $>2.6 \sigma$  detection significance levels. Therefore, J1521+5202 is considered to be detected in all Chandra observations. Note that productive spectral analyses are possible with the second and third observations despite the limited numbers of counts, since the signal-to-noise ratio is high with only 3–4 background counts expected in the source cell (see Table 1).

### 2.2. *XMM-Newton Observations*

Two XMM-Newton observations of J1521+5202 taken in July 2019 and December 2019 are listed in Table 1. The total observation times are 81 ks in July and 80 ks in December. The X-ray data were processed using the XMM-Newton Science Analysis System (SAS; Gabriel et al. 2004). We followed the standard procedure in the SAS Data Analysis Threads.<sup>1</sup> Background flares were filtered to generate cleaned event files. For each detector, source and background spectra were extracted with a  $10''$ -radius circular source region and a  $50''$ -radius circular source-free background region on the same CCD chip. Spectral response files were generated using the tasks RMFGEN and ARFGEN. For the July observation, the effective exposures in each detector are 42.1 ks in pn, 45.0 ks in MOS1, and 65.1 ks in MOS2. In (pn, MOS1, MOS2), we find (57, 31, 36) total counts (source+background) and (22.8, 10.4, 18.3) background-subtracted counts in the 0.5–10 keV energy range, and the total number of source counts in the three detectors is 51.5. For the December observation, the effective exposures in each detector are 46.6 ks in PN, 57.8 ks in MOS1, and 72.0 ks in MOS2. In (pn, MOS1, MOS2), we find (82, 38, 24) total counts (source+background) and (22.6, 24.0, 12.4) background-subtracted counts in the 0.5–10 keV energy range, and the total number of source counts in the three detectors is 59.0.

J1521+5202 was in a low-flux state during both XMM-Newton observations, and the resulting data have limited signal-to-noise ratios. Therefore, we will not attempt detailed spectral analyses of the XMM-Newton data beyond simple power-law spectral fitting.

## 3. X-RAY AND MULTIWAVELENGTH PROPERTIES

### 3.1. *Basic X-ray Spectral Analyses*

The rest-frame  $\approx 3 - 20$  keV Chandra and XMM-Newton spectra were fitted using *sherpa* (Freeman et al. 2001; Doe et al. 2007). The  $W$ -statistic was used due to the limited photon counts. The Galactic neutral hydrogen column density was fixed at  $1.58 \times 10^{20} \text{ cm}^{-2}$  (HI4PI Collaboration et al. 2016). To start, we adopted a simple power-law model modified by Galactic absorption to describe the 0.5–8 keV (for Chandra) or 0.5–10 keV (for XMM-Newton) spectra. The model was `phabs*zpowerlw`, where `zpowerlw` modeled the X-ray continuum, and `phabs` described the Galactic absorption. The effective power-law photon index derived

<sup>1</sup> <https://www.cosmos.esa.int/web/xmm-newton/sas-threads>.

**Table 1.** X-ray observation log

Observatory	Observation ID	Observation Start Date	Exposure Time (ks)	Net counts	Background counts
(1)	(2)	(3)	(4)	(5)	(6)
Chandra	6808	2006-07-16	4.1	2.8	0.3
	15334	2013-10-22	37.2	88.4	3.6
	27364	2023-02-02	29.7	111.0	3.1
XMM-Newton	0840440101	2019-07-26	42.1 (pn)	22.8 (pn)	34.2(pn)
	0840440201	2019-12-16	46.6 (pn)	22.6 (pn)	59.4 (pn)

NOTE—Column (1): Name of the X-ray observatory. Column (2): Observation ID. Column (3): Observation start date. Column (4): Cleaned exposure time. Column (5): Background-subtracted counts. Column (6): Background counts in the source cell.

from this modeling,  $\Gamma_{\text{eff}}$ , serves to characterize the basic spectral shape. We adopted a Monte Carlo approach to assess the goodness-of-fit (e.g., [Kaastra 2017](#)). The distribution of fit-statistic values is obtained by running simulations of the spectrum 10000 times using the best-fit model, instrument response, and exposure time. We also include parameter scatter in the simulations, where each input parameter set is one sampled realization of the fitting of the actual data. The fraction of simulated fit-statistic values smaller than our best-fit statistic value ( $P_{\text{rej}}$ ) represents the confidence level that the model can be rejected. The best-fit results are summarized in Table 2, and the best-fit model for the 2013 Chandra spectrum is shown in Figure 1(a). We also calculated  $\alpha_{\text{OX}}$  using the rest-frame 2 keV flux density ( $f_{2\text{ keV}}$ ) and rest-frame 2500 Å flux density ( $f_{2500\text{ Å}}$ ). The latter was converted from the  $r$ -band light curve (see Section 3.3 below). The  $\Delta\alpha_{\text{OX}}$  and  $f_{\text{weak}}$  values are also listed in Table 2, and J1521+5202 showed remarkable X-ray weakness ( $f_{\text{weak}} = 4.5\text{--}298$ ).

There appears to be substantial spectral variability of J1521+5202. The 2006 Chandra and 2019 XMM-Newton spectra have limited signal-to-noise ratios, and thus we focus the comparison on the 2013 and 2023 Chandra spectra. The large  $P_{\text{rej}}$  value for the 2013 spectrum (Table 2) suggests that the simple power-law model is inadequate to describe the data. However, given the difficulties in finding a better spectral model (see Section 3.2 below), we still consider that the power-law model provides a basic overall description of the spectral shape (via  $\Gamma_{\text{eff}}$ ) and flux level (via the normalization parameter) of the spectrum. In Figures 1(b) and 1(c), we show the unfolded best-fit power-law spectra and the 1–2 $\sigma$  contours of the  $\Gamma_{\text{eff}}$  and power-law

normalization parameters, respectively, demonstrating spectral variability between these two observations.

The small  $\Gamma_{\text{eff}}$  values (Table 2), compared to a typical value of  $\Gamma = 2.18 \pm 0.09$  for X-ray normal WLQs ([Luo et al. 2015](#)), indicate that the significant X-ray weakness of this source is likely due to strong absorption with Compton reflection also possibly present. Therefore, we further added an intrinsic-absorption component as a next step to fit the 2013 and 2023 Chandra spectra. The full model in `sherpa` was `phabs*zphabs*zpowerlw`, where `zphabs` accounted for the intrinsic absorption. For the 2013 observation, the best-fit  $\Gamma = 1.5^{+0.4}_{-0.3}$ , and  $N_{\text{H}} = (1.3^{+0.6}_{-0.5}) \times 10^{23} \text{ cm}^{-2}$ . For the 2023 observation, the best-fit  $\Gamma = 3.1^{+0.5}_{-0.5}$ , and  $N_{\text{H}} = (5.3^{+1.4}_{-1.7}) \times 10^{23} \text{ cm}^{-2}$  (Figure 1). The  $P_{\text{rej}}$  are 99.6% and 27.9% for the 2013 and 2023 fits, respectively. After considering intrinsic absorption, the two observations’ best-fit  $\Gamma$  values were still inconsistent with each other and the typical  $\Gamma$  values of X-ray normal WLQs ( $2.18 \pm 0.09$ ). Therefore, we further fixed the  $\Gamma$  at 2.18 to assess what this implied for the intrinsic  $N_{\text{H}}$  and normalization. The best-fit  $N_{\text{H}}$  values were  $(2.2^{+0.4}_{-0.4}) \times 10^{23} \text{ cm}^{-2}$  in the 2013 observation and  $(3.0^{+0.7}_{-0.6}) \times 10^{23} \text{ cm}^{-2}$  in the 2023 observation. Besides, the normalization of the `zpowerlw` model increased by a factor of 2.5 from 2013 to 2023 with  $\Gamma$  fixed at 2.18. The best-fit results are summarized in Table 3, and the best-fit model for the 2023 Chandra spectrum is shown in Figure 1(d). The  $P_{\text{rej}}$  are 99.8% and 20.7% for the 2013 and 2023 fits, respectively, and the high  $P_{\text{rej}}$  for 2013 suggests additional spectral complexity may be present. For the 2023 observation, we calculate the absorption-corrected  $\alpha_{\text{OX,corr}} = -1.80^{+0.02}_{-0.02}$  and  $\Delta\alpha_{\text{OX,corr}} = 0.03$  with  $\Gamma$  fixed at 2.18, indicating that J1521+5202 emit

ted a nominal intrinsic level of X-ray emission relative to its optical/UV emission at this epoch.

### 3.2. Testing of Additional X-ray Spectral Models

The relatively poor fit-quality results for the 2013 spectrum of J1521+5202 in Section 3.1 suggest that additional spectral complexity was present at this epoch. We have therefore attempted to fit the 2013 spectrum with a variety of spectral models, including a partially covering absorption model, a double-absorber model, a broken power-law model with absorption, and Compton-thick absorption models. Unfortunately, none of the models tested provides a statistically meaningful improvement in fit quality as assessed using simulations; e.g., the  $P_{\text{rej}}$  we obtain is 99.7% for the double-absorber model. The lack of improvement in fit quality can be partly understood from the lack of strong systematic residuals in Figure 1(a), where the data points appear generally scattered around the best fit but without a clear systematic trend that can be straightforwardly modeled. There is likely additional spectral complexity present in 2013, but with only 88 net counts, we are unable to constrain robustly the nature of this complexity. Furthermore, the strong spectral variability between 2013 and 2023 makes it difficult to use the 2023 X-ray spectrum as a guide for interpreting the 2013 spectrum better.

The strong X-ray weakness and hard X-ray spectral shape of J1521+5202 during 2013 suggest that heavy X-ray obscuration is present. It is therefore worth testing if the 2013 spectrum is dominated by Compton reflection, which could occur if the direct line-of-sight absorption column density toward the nuclear X-ray source is Compton thick. If J1521+5202 were found to have Compton-thick absorption, it would be among the most-luminous Compton-thick quasars in the Universe with a bolometric luminosity comparable to the powerful obscured AGNs in the most-luminous hot dust-obscured galaxies (hot DOGs; e.g., Vito et al. 2018).

We have tested if the 2013 spectrum from rest-frame 3–20 keV is dominated by Compton reflection using the BORUS model for Compton reflection from the obscuring tori of AGNs (Baloković et al. 2018). Specifically, we tried the following model: `phabs*borus`, where `borus` is the reprocessed torus emission model of Baloković et al. (2018). We fixed the  $N_{\text{H}}$  value of BORUS at  $1 \times 10^{25} \text{ cm}^{-2}$ , corresponding to highly Compton-thick material. This model does not fit the data well; the  $P_{\text{rej}}$

is 99.99%. The primary reason this Compton-reflection dominated model fails to fit the data is that the predicted 3–20 keV continuum is even harder than what is observed, owing to the rapid spectral rise toward the peak of the Compton-reflection hump at 20–30 keV.

The BORUS model is derived for the case of Compton reflection from a standard torus of AGN unified schemes, while the obscuring material for WLQs is likely the TDO (see Section 1.1). The TDO is expected to be more highly ionized than a standard torus, and it also will have rotational and/or outflow motions. Therefore, we have also considered the case of Compton reflection from an ionized medium using the RELXILL model of Dauser et al. (2014) and García et al. (2014), which incorporates XILLVER and RELCONV. The former calculates the reflection in the rest frame of an accretion disk, and the latter models the relativistic convolution. We tried the following model: `phabs*relxill`. We fixed the reflection fraction to  $-1$  to model a reflection-dominated situation.<sup>2</sup> The disk ionization parameter ( $\xi$ ) is defined as  $\xi = 4\pi F_{\text{ion}}/n$ , in units of  $\text{erg cm s}^{-1}$ , where  $F_{\text{ion}}$  is the ionizing irradiating flux, and  $n$  is the number density of the disk. RELXILL allows  $\log \xi$  to vary between 0 (neutral) and 4.7 (highly ionized). Our best-fit  $\log \xi = 1.7$ , corresponding to a moderately ionized accretion disk. The  $P_{\text{rej}}$  is 98.2%. RELXILL somewhat improves the fit quality, predicting a softer spectrum than BORUS, but it is still unacceptable considering the high  $P_{\text{rej}}$  and similar residuals to those in Figure 1(a) without a clear systematic trend. While the RELXILL model is still likely not optimal for modeling the reflection from a TDO, our basic tests with it indicate that ionized reflection is unlikely to provide a satisfactory fit for the 2013 spectrum.

In 2023, we note J1521+5202 is only X-ray weak by a factor of  $\approx 4$  and has a softer observed continuum shape (see Table 2). Thus, Compton-thick absorption and Compton reflection are unlikely to be relevant in 2023, and this is confirmed by our spectral-fitting tests.

### 3.3. Spectral Energy Distribution and Light Curves

In Figure 2, we show the IR-to-X-ray SED for J1521+5202. The IR-optical measurements are collected from the Wide-field Infrared Survey Explorer (WISE; Wright et al. 2010), Near-Earth Object WISE Reactivation (NEOWISE; Mainzer et al. 2011), Sloan Digital Sky Survey (SDSS; York et al. 2000), Zwicky Transient Facility (ZTF; Bellm et al. 2019), and

<sup>2</sup> We assumed a power-law disk emissivity profile and fixed the dimensionless black-hole spin at 0.2 for simplicity. These parameters cannot be meaningfully constrained with our data.

**Table 2.** Best-fit results with a power-law model

Observation	$\Gamma_{\text{eff}}$	$\log F_X$	$f_{2\text{ keV}}$	$f_{2500\text{ \AA}}$	$\alpha_{\text{OX}}$	$\Delta\alpha_{\text{OX}}$	$f_{\text{weak}}$	$W/d.o.f.$	$P_{\text{rej}}$
Time[year]	(0.5–2 keV)								
(1)	(2)	(3)	(4)	(5)	(6)	(7)	(8)	(9)	(10)
Chandra [2006]	$-0.1^{+1.3}_{-1.0}$	$-14.8^{+0.3}_{-0.4}$	$0.2^{+0.7}_{-0.2}$	24.4	$-2.70^{+0.5}_{-0.2}$	-0.86	$180^{+404}_{-165}$	0.04/1	12.9%
Chandra [2013]	$0.7^{+0.2}_{-0.2}$	$-14.3^{+0.1}_{-0.1}$	$1.2^{+0.4}_{-0.3}$	22.3	$-2.40^{+0.05}_{-0.04}$	-0.56	$30^{+8}_{-7}$	104.6/76	99.7%
XMM-Newton [2019-07]	$0.4^{+0.4}_{-0.4}$	$-15.2^{+0.2}_{-0.2}$	$0.11^{+0.08}_{-0.05}$	18.6	$-2.77^{+0.12}_{-0.08}$	-0.95	$298^{+184}_{-153}$	104.3/114	76.1%
XMM-Newton [2019-12]	$0.9^{+0.4}_{-0.4}$	$-15.1^{+0.1}_{-0.2}$	$0.19^{+0.12}_{-0.08}$	18.4	$-2.68^{+0.11}_{-0.07}$	-0.86	$195^{+107}_{-84}$	148.1/132	96.5%
Chandra [2023]	$1.4^{+0.2}_{-0.2}$	$-13.7^{+0.1}_{-0.1}$	$7.5^{+3.8}_{-2.6}$	19.4	$-2.08^{+0.08}_{-0.06}$	-0.25	$4.5^{+1.9}_{-1.7}$	80.7/85	66.2%

NOTE—Column (1): Observatory and observation year. Column (2): 0.5–8 keV effective power-law photon index. Column (3): Galactic absorption-corrected logarithm of observed-frame 0.5–2 keV flux. Column (4): Rest-frame 2 keV flux density in units of  $10^{-32}$  erg  $\text{cm}^{-2}\text{s}^{-1}\text{Hz}^{-1}$ . Column (5): Flux density at rest-frame 2500 Å converted from the  $r$ -band light curve (Section 3.3) in units of  $10^{-27}$  erg  $\text{cm}^{-2}\text{s}^{-1}\text{Hz}^{-1}$ . Column (6): Measured  $\alpha_{\text{OX}}$  parameter. Column (7): The difference between the measured  $\alpha_{\text{OX}}$  and the expected  $\alpha_{\text{OX}}$  from the  $\alpha_{\text{OX}}-L_{2500\text{ \AA}}$  relation in Just et al. (2007). Column (8): Factor of X-ray weakness. Column (9):  $W$ -statistic over degrees of freedom. Column (10): The fraction of simulated fit-statistic values smaller than our best-fit statistic value, representing the confidence level that the model can be rejected.

**Table 3.** Best-fit results with an absorbed power-law model

Observation	$\Gamma$	$N_{\text{H}}$	Norm	$W/d.o.f.$	$P_{\text{rej}}$
year	$(10^{23}\text{ cm}^{-2})$				
(1)	(2)	(3)	(4)	(5)	(6)
Chandra [2013]	$1.5^{+0.4}_{-0.3}$	$1.3^{+0.6}_{-0.5}$	$0.4^{+0.5}_{-0.2}$	95.5/75	99.6%
Chandra [2023]	$3.1^{+0.5}_{-0.5}$	$5.3^{+1.4}_{-1.7}$	$43^{+114}_{-30}$	62.5/84	27.9%
Chandra [2013]	2.18 (fixed)	$2.2^{+0.4}_{-0.4}$	$1.8^{+0.3}_{-0.3}$	98.5/76	99.8%
Chandra [2023]	2.18 (fixed)	$3.0^{+0.7}_{-0.6}$	$4.4^{+0.7}_{-0.6}$	66.2/85	20.7%

NOTE— $\Gamma$  is a free parameter in the first two rows and is fixed at 2.18 in the last two rows. Column (1): Observatory and observation year. Column (2): Power-law photon index. Column (3): Intrinsic absorption column density. Column (4): Power-law normalization in units of  $10^{-4}$  photons  $\text{cm}^{-2}\text{s}^{-1}\text{keV}^{-1}$ . Column (5):  $W$ -statistic over degrees of freedom. Column (6): The fraction of simulated fit-statistic values smaller than our best-fit statistic value, representing the confidence level that the model can be rejected.

Catalina Real-Time Transient Survey (CRTS; Drake et al. 2009). We plotted the average measurements of multi-epoch observations for the NEOWISE, ZTF, and CRTS data. All SED data and light curves have been corrected for Galactic extinction using the extinction law in Fitzpatrick et al. (2019) with  $R_V = 3.1$ . The Galactic  $E(B - V)$  value of J1521+5202 was 0.019 (Schlegel et al. 1998). We did not present observed UV data for J1521+5202 because the strong intergalactic medium absorption made these points uncertain. We added the 2 keV luminosity determined from the best-

fit results in Table 2. For comparison, we included the mean SED of high-luminosity quasars in Krawczyk et al. (2013), scaled to the 2500 Å luminosity. The IR–optical SED of J1521+5202 was broadly consistent with those of typical luminous quasars. However, this quasar showed remarkable X-ray weakness in most epochs and X-ray variability.

The IR–optical light curves are shown in panels (a), (b), and (c) of Figure 3, obtained from the NEOWISE, ZTF, and CRTS catalogs. The observed-frame 0.5–2 keV flux ( $F_X$ ) and  $\alpha_{\text{OX}}$  derived from Table 2

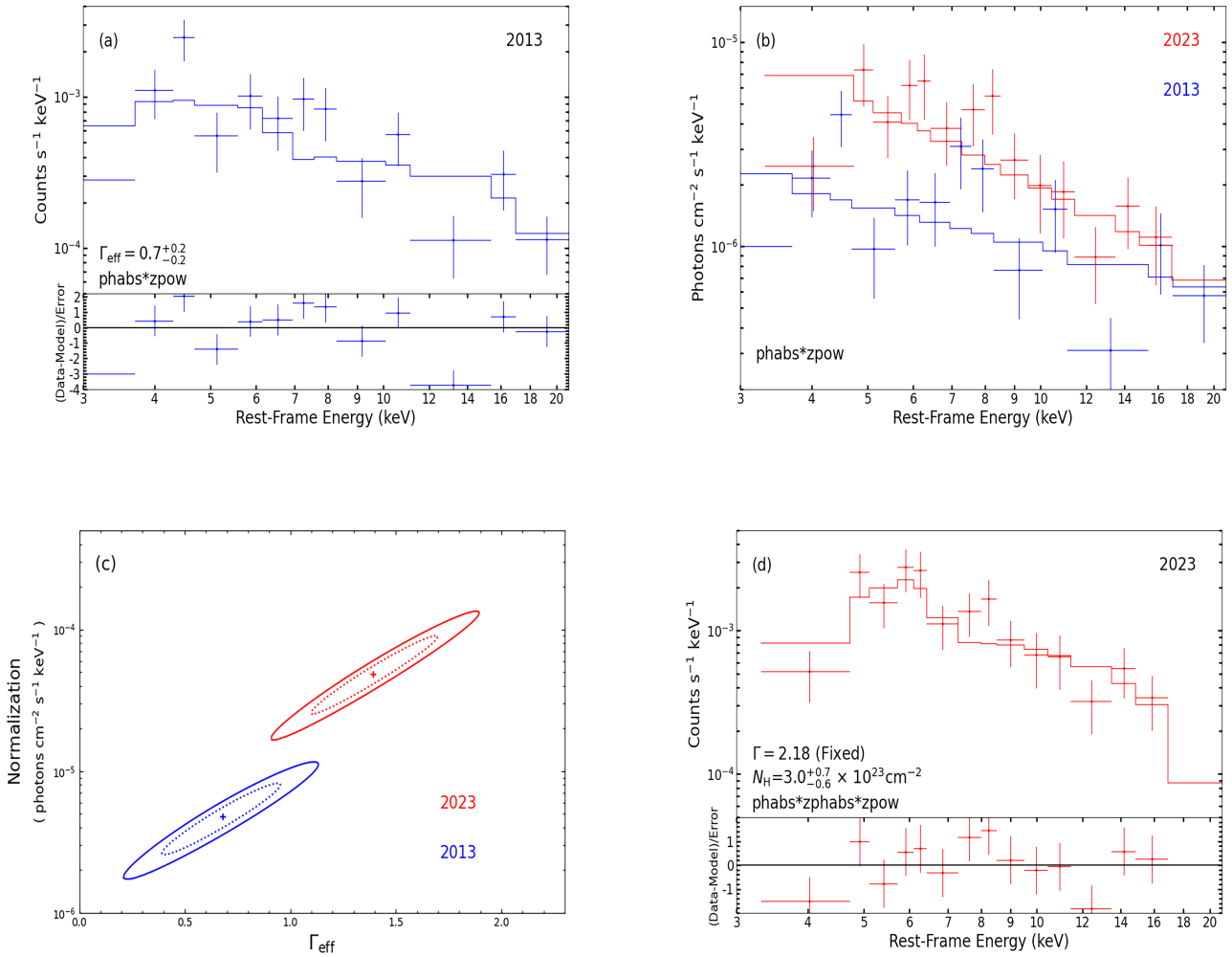


**Figure 1.** (a): Chandra 2013 spectrum overlaid with the best-fit simple power-law model. The bottom panel displays the fitting residuals. The data are grouped for display purposes only. (b): Unfolded Chandra 2013 (blue) and 2023 (red) spectra overlaid with the best-fit simple power-law models, showing the spectral shape and flux variations between the two spectra. (c): The  $\Gamma_{\text{eff}}$  and normalization values (blue and red plus symbols) and their  $1\sigma$  (dotted) and  $2\sigma$  (solid) contours for the best-fit simple power-law models. (d): Chandra 2023 spectrum overlaid with the best-fit absorbed power-law model. The bottom panel displays the fitting residuals.

are shown in panels (d) and (e), respectively. For the IR–optical light curves, we grouped any intraday measurements. We converted the CRTS magnitudes to ZTF  $g$ - and  $r$ -band magnitudes using the filter transmission and SDSS spectrum. We also computed the conversion uncertainty from CRTS to ZTF. The uncertainty caused by the deviation of the optical continuum power-law index was 0.01 mag in the  $r$ -band and 0.02 mag in the  $g$ -band. The cross-instrument uncertainty was 0.24 mag in the  $r$ -band and 0.25 mag in the  $g$ -band. In panels (b) and (c), we also included the SDSS  $g$ - and  $r$ -band photometric measurements. In panel (a), the maximum variability amplitude in the W1 band ( $3.4 \mu\text{m}$ ) reached  $\approx 0.1$

mag ( $\approx 10\%$ ). In panels (b) and (c), the maximum long-term optical variability amplitudes reached  $\approx 0.4$  mag ( $\approx 45\%$ ) in the  $r$ -band and  $\approx 0.8$  mag ( $\approx 100\%$ ) in the  $g$ -band. In panel (d), the largest variability amplitude of  $F_X$  was observed between the 2019 XMM-Newton observation and the 2023 Chandra observation and reached a factor of  $32^{+31}_{-16}$ , showing strong X-ray variability in 0.97 rest-frame years. Such large long-term X-ray variability amplitudes are rare among quasars (e.g., Yang et al. 2016; Middei et al. 2017; Timlin et al. 2020). Following Section 4.2 of Timlin et al. (2020), this variation was a  $\approx 7.6 \sigma_{\text{MAD}}$  event, where  $\sigma_{\text{MAD}}$  is a robust estima-

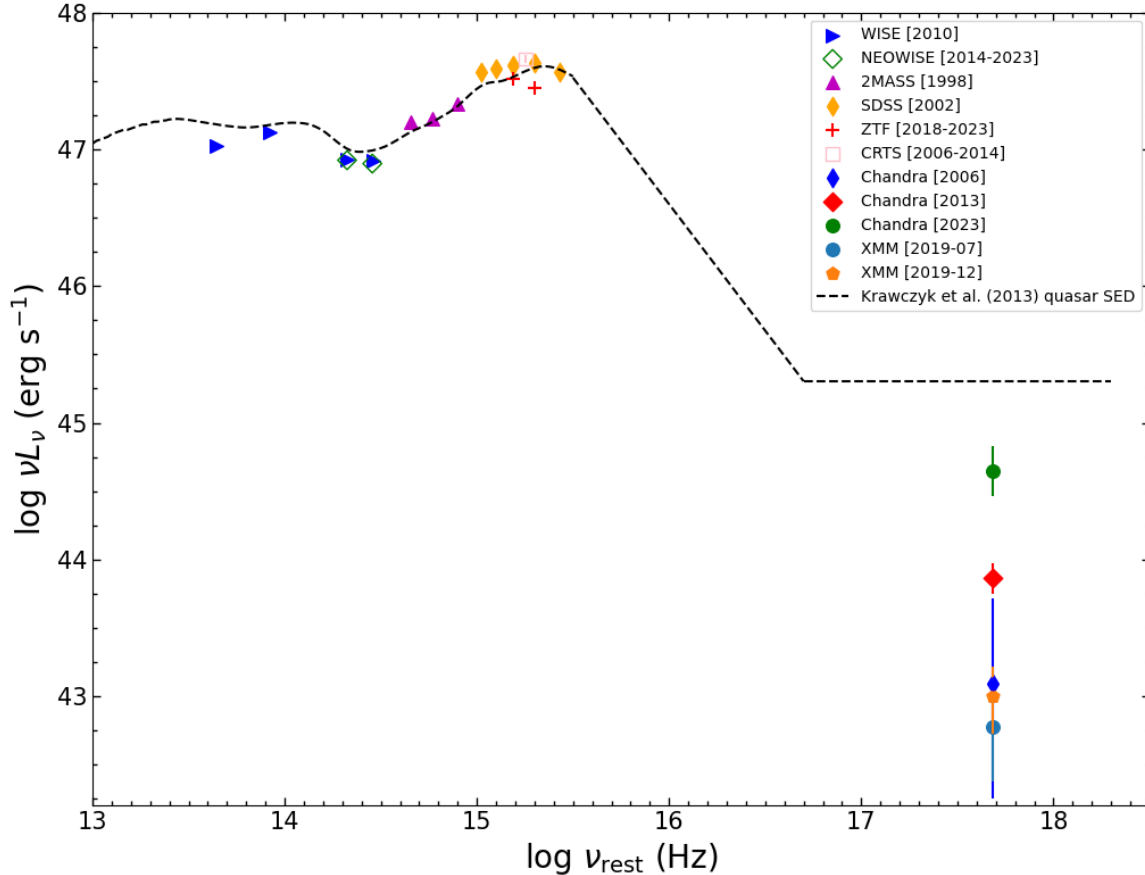


**Figure 2.** IR-to-X-ray SED for J1521+5202. IR-to-optical data points are obtained from the WISE, NEOWISE, 2MASS, ZTF, and CRTS catalogs, where the NEOWISE, ZTF, and CRTS data points show average measurements of multi-epoch observations. The rest-frame 2 keV luminosities are taken from Table 2. The dashed curve shows the mean luminous quasar SED from Krawczyk et al. (2013) normalized to the 2500 Å luminosity; the X-ray component is a  $\Gamma = 2$  power-law continuum with 2 keV luminosity determined from the  $\alpha_{\text{OX}}-L_{2500\text{\AA}}$  relation in Just et al. (2007) ( $f_{\text{weak}}=0$ ).

tor of the standard deviation derived using the median absolute deviation (MAD).

#### 4. SUMMARY AND FUTURE WORK

We have reported on the X-ray spectra and variability of the optically ultraluminous WLQ J1521+5202 observed by Chandra and XMM-Newton. The key observational findings are the following:

1. J1521+5202 shows remarkable X-ray weakness and small  $\Gamma_{\text{eff}}$  values in all X-ray observations spanning 17 years, indicating consistently strong X-ray absorption. See Section 3.1.
2. The 2023 Chandra spectrum can be acceptably described by a power law modified by heavy intrinsic

absorption, but this model does not fit the 2013 spectrum well. See Sections 3.1 and 3.2.

3. J1521+5202 has a typical quasar IR-to-optical SED, and the long-term IR/optical variability amplitudes are mild (e.g., a maximum variability amplitude of  $\approx 45\%$  in the  $r$ -band). However, this quasar shows remarkable concurrent X-ray flux and spectral variability. For example, the observed-frame 0.5–2 keV flux varies by a factor of  $32^{+31}_{-16}$  in 0.97 rest-frame years between the 2019 XMM-Newton observation and the 2023 Chandra observation. See Section 3.3.

The overall X-ray and multiwavelength properties of J1521+5202 are qualitatively consistent with expectations for the TDO model, where the large X-ray varia-



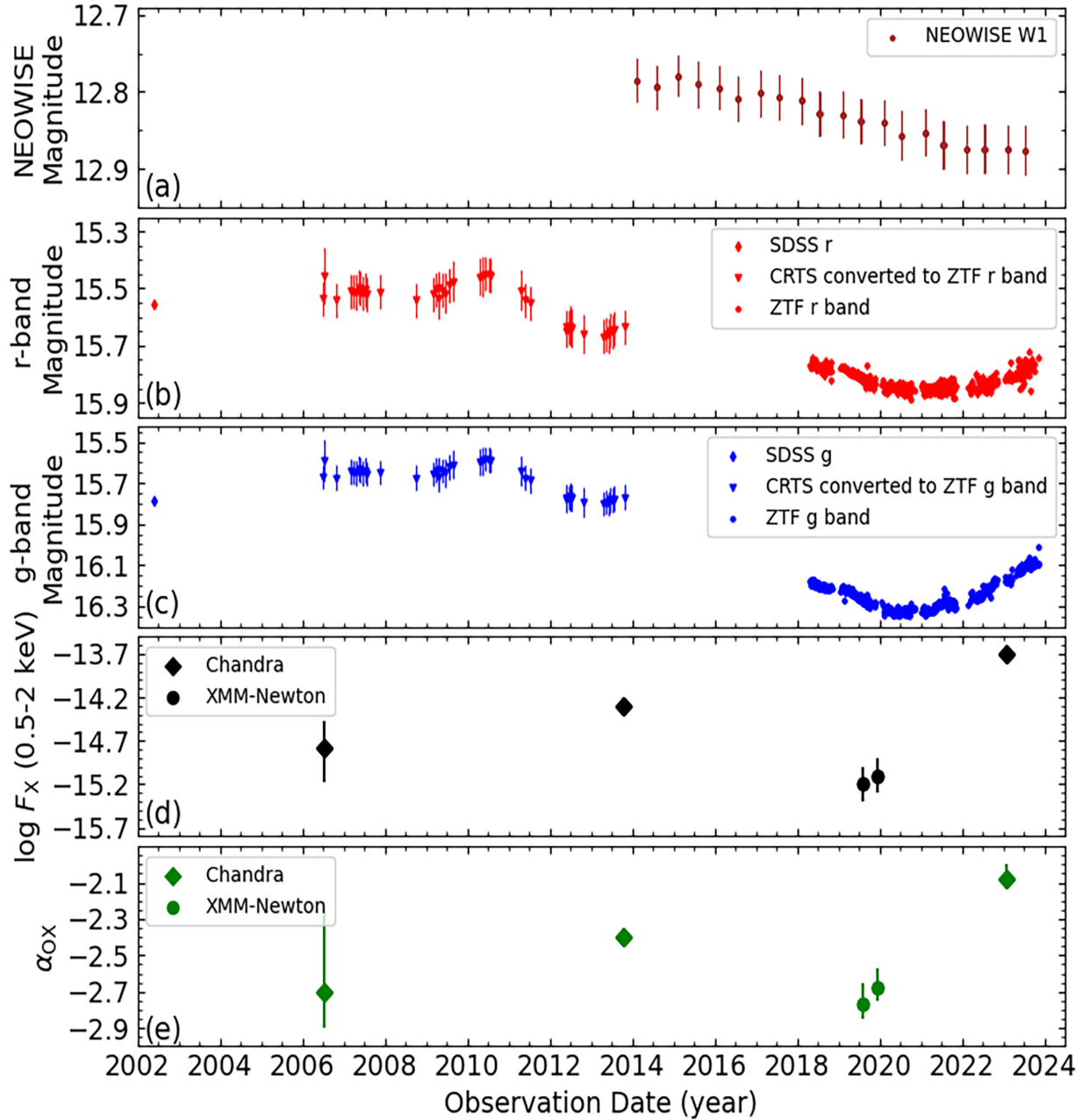


**Figure 3.** Light curves for the (a) NEOWISE W1 band ( $3.4 \mu\text{m}$ ), (b) ZTF  $r$ -band, (c) ZTF  $g$ -band, (d) observed-frame 0.5–2 keV band (note the logarithmic scaling), and (e)  $\alpha_{OX}$ . We group intraday measurements and convert the CRTS magnitude to ZTF  $g$ -band and  $r$ -band magnitudes using the filter transmission curves and SDSS spectrum.

tions could be driven by changes in the column density and/or the covering factor of the TDO, as the wind is a highly dynamical structure that would likely change on the observed multi-year timescales substantially. Besides, optical/UV photons produced on larger scales in the accretion disk remain largely unobscured (see Figure 1 of Ni et al. 2018), and one would likely expect modest IR/optical variability much like that of a typical quasar, which is consistent with our IR-optical SED and light curves (Figure 3). In this scenario, the line-of-sight X-ray absorption by the TDO would be strong during the 2013 Chandra observation and even stronger during the 2019 XMM-Newton observations, and then it would drop greatly by the time of the 2023 Chandra observation. The intrinsically nominal level of X-ray emission relative to the optical/UV emission inferred from the 2023 Chandra spectrum (Section 3.1) supports this scenario. Unfortunately, the other X-ray spectra do not allow us to determine reliably any absorption parameters (see Sections 3.1 and 3.2), and it is not clear whether it was variations of the TDO column density or TDO covering factor that drove the X-ray variability. The fact that a Compton-reflection model does not fit the 2013 Chandra spectrum well indicates that the thick disk itself, which is expected to be highly Compton thick, is probably not lying along our line-of-sight. Rather, at least in the case of J1521+5202, the outflow from the thick disk is probably what lies along our line-of-sight.

The general similarity of the X-ray variability of J1521+5202 to that of other WLQs with apparent TDO variations, including PHL 1092 (Miniutti et al. 2012), SDSS J1539+3954 (Ni et al. 2020), and SDSS J1350+2618 (Liu et al. 2022), also supports an absorption-variability interpretation. The extensively studied low-redshift ( $z = 0.18$ ) quasar PDS 456 also has C IV properties similar to those of WLQs (e.g., O’Brien et al. 2005) and shows impressive X-ray absorption and luminosity changes (e.g., Reeves et al. 2020, 2021).

The remarkable X-ray spectral and variability properties of J1521+5202 and X-ray weak WLQs generally require more photons per epoch for detailed study. This would require expensive Chandra or XMM-Newton observations (hundreds of ks per epoch). Furthermore, these observations would have risk owing to the strong X-ray variability of J1521+5202; note this strong variability already negatively impacted the 161 ks of XMM-Newton observations in 2021. Next-generation X-ray observatories, including Athena (Nandra et al. 2013) and Lynx (Gaskin et al. 2019), will have photon-collecting areas at least an order-of-magnitude larger than for Chandra, and thus would allow much more efficient spectroscopic and variability investigations of J1521+5202 and related WLQs. If Athena and Lynx can maintain flexible observation scheduling, then a short observation could be obtained to check the flux level efficiently and decide if a proximate longer spectroscopic observation is merited.

SW acknowledges financial support from Nanjing University. WNB, ZY, and FZ acknowledge financial support from Chandra X-ray Center grant GO2-23083X, the Penn State Eberly Endowment, and Penn State ACIS Instrument Team Contract SV4-74018 (issued by the Chandra X-ray Center, which is operated by the Smithsonian Astrophysical Observatory for and on behalf of NASA under contract NAS8-03060). BL acknowledges financial support from the National Natural Science Foundation of China grant 11991053. The Chandra ACIS Team Guaranteed Time Observations (GTO) utilized were selected by the ACIS Instrument Principal Investigator, Gordon P. Garmire, currently of the Huntingdon Institute for X-ray Astronomy, LLC, which is under contract to the Smithsonian Astrophysical Observatory via Contract SV2-82024.

## REFERENCES

- Baloković, M., Brightman, M., Harrison, F. A., et al. 2018, *ApJ*, 854, 42, doi: [10.3847/1538-4357/aaa7eb](https://doi.org/10.3847/1538-4357/aaa7eb)
- Bellm, E. C., Kulkarni, S. R., Graham, M. J., et al. 2019, *PASP*, 131, 018002, doi: [10.1088/1538-3873/aaecbe](https://doi.org/10.1088/1538-3873/aaecbe)
- Dauser, T., Garcia, J., Parker, M. L., Fabian, A. C., & Wilms, J. 2014, *MNRAS*, 444, L100, doi: [10.1093/mnrasl/slu125](https://doi.org/10.1093/mnrasl/slu125)
- Diamond-Stanic, A. M., Fan, X., Brandt, W. N., et al. 2009, *ApJ*, 699, 782, doi: [10.1088/0004-637X/699/1/782](https://doi.org/10.1088/0004-637X/699/1/782)
- Doe, S., Nguyen, D., Stawarz, C., et al. 2007, in *Astronomical Society of the Pacific Conference Series*, Vol. 376, *Astronomical Data Analysis Software and Systems XVI*, ed. R. A. Shaw, F. Hill, & D. J. Bell, 543
- Drake, A. J., Djorgovski, S. G., Mahabal, A., et al. 2009, *ApJ*, 696, 870, doi: [10.1088/0004-637X/696/1/870](https://doi.org/10.1088/0004-637X/696/1/870)
- Fan, X., Strauss, M. A., Gunn, J. E., et al. 1999, *ApJL*, 526, L57, doi: [10.1086/312382](https://doi.org/10.1086/312382)
- Fitzpatrick, E. L., Massa, D., Gordon, K. D., Bohlin, R., & Clayton, G. C. 2019, *ApJ*, 886, 108, doi: [10.3847/1538-4357/ab4c3a](https://doi.org/10.3847/1538-4357/ab4c3a)

- Freeman, P., Doe, S., & Siemiginowska, A. 2001, in *Society of Photo-Optical Instrumentation Engineers (SPIE) Conference Series*, Vol. 4477, *Astronomical Data Analysis*, ed. J.-L. Starck & F. D. Murtagh, 76–87, doi: [10.1117/12.447161](https://doi.org/10.1117/12.447161)
- Gabriel, C., Denby, M., Fyfe, D. J., et al. 2004, in *Astronomical Society of the Pacific Conference Series*, Vol. 314, *Astronomical Data Analysis Software and Systems (ADASS) XIII*, ed. F. Ochsenbein, M. G. Allen, & D. Egret, 759
- García, J., Dauser, T., Lohfink, A., et al. 2014, *ApJ*, 782, 76, doi: [10.1088/0004-637X/782/2/76](https://doi.org/10.1088/0004-637X/782/2/76)
- Gaskin, J. A., Swartz, D. A., Vikhlinin, A., et al. 2019, *Journal of Astronomical Telescopes, Instruments, and Systems*, 5, 021001, doi: [10.1117/1.JATIS.5.2.021001](https://doi.org/10.1117/1.JATIS.5.2.021001)
- HI4PI Collaboration, Ben Bekhti, N., Flöer, L., et al. 2016, *A&A*, 594, A116, doi: [10.1051/0004-6361/201629178](https://doi.org/10.1051/0004-6361/201629178)
- Just, D. W., Brandt, W. N., Shemmer, O., et al. 2007, *ApJ*, 665, 1004, doi: [10.1086/519990](https://doi.org/10.1086/519990)
- Kaastra, J. S. 2017, *A&A*, 605, A51, doi: [10.1051/0004-6361/201629319](https://doi.org/10.1051/0004-6361/201629319)
- Krawczyk, C. M., Richards, G. T., Mehta, S. S., et al. 2013, *ApJS*, 206, 4, doi: [10.1088/0067-0049/206/1/4](https://doi.org/10.1088/0067-0049/206/1/4)
- Liu, H., Luo, B., Brandt, W. N., et al. 2022, *ApJ*, 930, 53, doi: [10.3847/1538-4357/ac6265](https://doi.org/10.3847/1538-4357/ac6265)
- Luo, B., Brandt, W. N., Hall, P. B., et al. 2015, *ApJ*, 805, 122, doi: [10.1088/0004-637X/805/2/122](https://doi.org/10.1088/0004-637X/805/2/122)
- Mainzer, A., Bauer, J., Grav, T., et al. 2011, *ApJ*, 731, 53, doi: [10.1088/0004-637X/731/1/53](https://doi.org/10.1088/0004-637X/731/1/53)
- Marlar, A., Shemmer, O., Anderson, S. F., et al. 2018, in *American Astronomical Society Meeting Abstracts*, Vol. 232, *American Astronomical Society Meeting Abstracts #232*, 318.10
- Middei, R., Vagnetti, F., Bianchi, S., et al. 2017, *A&A*, 599, A82, doi: [10.1051/0004-6361/201629940](https://doi.org/10.1051/0004-6361/201629940)
- Miniutti, G., Brandt, W. N., Schneider, D. P., et al. 2012, *MNRAS*, 425, 1718, doi: [10.1111/j.1365-2966.2012.21648.x](https://doi.org/10.1111/j.1365-2966.2012.21648.x)
- Nandra, K., Barret, D., Barcons, X., et al. 2013, arXiv e-prints, arXiv:1306.2307, doi: [10.48550/arXiv.1306.2307](https://doi.org/10.48550/arXiv.1306.2307)
- Ni, Q., Brandt, W. N., Luo, B., et al. 2018, *MNRAS*, 480, 5184, doi: [10.1093/mnras/sty1989](https://doi.org/10.1093/mnras/sty1989)
- Ni, Q., Brandt, W. N., Yi, W., et al. 2020, *ApJL*, 889, L37, doi: [10.3847/2041-8213/ab6d78](https://doi.org/10.3847/2041-8213/ab6d78)
- Ni, Q., Brandt, W. N., Luo, B., et al. 2022, *MNRAS*, 511, 5251, doi: [10.1093/mnras/stac394](https://doi.org/10.1093/mnras/stac394)
- O’Brien, P. T., Reeves, J. N., Simpson, C., & Ward, M. J. 2005, *MNRAS*, 360, L25, doi: [10.1111/j.1745-3933.2005.00038.x](https://doi.org/10.1111/j.1745-3933.2005.00038.x)
- Reeves, J. N., Braitto, V., Chartas, G., et al. 2020, *ApJ*, 895, 37, doi: [10.3847/1538-4357/ab8cc4](https://doi.org/10.3847/1538-4357/ab8cc4)
- Reeves, J. N., Braitto, V., Porquet, D., et al. 2021, *MNRAS*, 500, 1974, doi: [10.1093/mnras/staa3377](https://doi.org/10.1093/mnras/staa3377)
- Schlegel, D. J., Finkbeiner, D. P., & Davis, M. 1998, *ApJ*, 500, 525, doi: [10.1086/305772](https://doi.org/10.1086/305772)
- Schneider, D. P., Hall, P. B., Richards, G. T., et al. 2005, *AJ*, 130, 367, doi: [10.1086/431156](https://doi.org/10.1086/431156)
- Steffen, A. T., Strateva, I., Brandt, W. N., et al. 2006, *AJ*, 131, 2826, doi: [10.1086/503627](https://doi.org/10.1086/503627)
- Timlin, John D., I., Brandt, W. N., Zhu, S., et al. 2020, *MNRAS*, 498, 4033, doi: [10.1093/mnras/staa2661](https://doi.org/10.1093/mnras/staa2661)
- Vito, F., Brandt, W. N., Stern, D., et al. 2018, *MNRAS*, 474, 4528, doi: [10.1093/mnras/stx3120](https://doi.org/10.1093/mnras/stx3120)
- Wright, E. L., Eisenhardt, P. R. M., Mainzer, A. K., et al. 2010, *AJ*, 140, 1868, doi: [10.1088/0004-6256/140/6/1868](https://doi.org/10.1088/0004-6256/140/6/1868)
- Wu, J., Brandt, W. N., Anderson, S. F., et al. 2012, *ApJ*, 747, 10, doi: [10.1088/0004-637X/747/1/10](https://doi.org/10.1088/0004-637X/747/1/10)
- Wu, J., Brandt, W. N., Hall, P. B., et al. 2011, *ApJ*, 736, 28, doi: [10.1088/0004-637X/736/1/28](https://doi.org/10.1088/0004-637X/736/1/28)
- Yang, G., Brandt, W. N., Luo, B., et al. 2016, *ApJ*, 831, 145, doi: [10.3847/0004-637X/831/2/145](https://doi.org/10.3847/0004-637X/831/2/145)
- York, D. G., Adelman, J., Anderson, John E., J., et al. 2000, *AJ*, 120, 1579, doi: [10.1086/301513](https://doi.org/10.1086/301513)